

Article

Estimation of Reverse Flow Rate in J-Groove Channel of AJP and SCP Models Using CFD Analysis

Ujjwal Shrestha ¹  and Young-Do Choi ^{2,*} 

¹ Graduate School of Mechanical Engineering, Mokpo National University, Muan 58554, Korea; d19541301@365.mokpo.ac.kr

² Department of Mechanical Engineering, Institute of New and Renewable Energy Technology Research, Mokpo National University, Muan 58554, Korea

* Correspondence: ydchoi@mnu.ac.kr

Abstract: An annular jet pump (AJP) and a screw centrifugal pump (SCP) are special-purpose pumps used for transportation. The flow fields in the AJP and SCP are like those in a diffuser without and with an impeller, respectively. The flow from diffuser inlet to outlet takes place via the conversion of kinetic energy to static pressure. J-Groove is installed in the diffuser wall of an AJP and SCP to induce reverse flow from the diffuser outlet to the inlet, which suppresses the cavitation. CFD analysis was carried out to verify the conceptual design and understand the internal flow field of an AJP and SCP with J-Groove. The CFD analysis showed that the J-Groove installation in the AJP and SCP improved suction performance. The reverse flow in the J-Groove is due to the pressure difference between the diffuser outlet and the inlet. The numerical analysis results showed that the reverse flow mechanism is dependent on the flow conditions, cavitation number, and presence of the impeller. In a higher flow rate, the reverse flow rate is higher in the AJP model and lower in the SCP model and vice versa. Finally, CFD analysis concluded that the reverse flow rate in J-Groove improves the suction performance of the AJP and SCP models.

Keywords: annular jet pump (AJP); screw centrifugal pump (SCP); J-Groove (JG); reverse flow rate; suction performance



Citation: Shrestha, U.; Choi, Y.-D. Estimation of Reverse Flow Rate in J-Groove Channel of AJP and SCP Models Using CFD Analysis. *Processes* **2022**, *10*, 785. <https://doi.org/10.3390/pr10040785>

Academic Editor: Lei Tan

Received: 11 March 2022

Accepted: 13 April 2022

Published: 16 April 2022

Publisher's Note: MDPI stays neutral with regard to jurisdictional claims in published maps and institutional affiliations.



Copyright: © 2022 by the authors. Licensee MDPI, Basel, Switzerland. This article is an open access article distributed under the terms and conditions of the Creative Commons Attribution (CC BY) license (<https://creativecommons.org/licenses/by/4.0/>).

1. Introduction

With the growth in the agriculture and aquaculture industry, the demand for transportation pumps has increased. The pumps can be efficient and effective substitutes for transportation. Among various pump categories, jet pumps and screw centrifugal pumps are used in sewage transfer, petroleum, metallurgy, and other industries for transportation [1,2]. Therefore, jet pumps and centrifugal pumps are the most viable options to solve the transportation problem of sensitive goods such as vegetables and live fish.

Jet pumps are preferred for transportation because they are simple in design without rotating and reciprocating components, low cost, and have desirable mass transfer [3,4]. The primary and secondary inlets, nozzle, diffuser, and outlet are the main components of a jet pump. A jet pump converts pressure energy into kinetic energy using a nozzle and diffuser. The high pressurized primary flow passes through the nozzle and increases the fluid velocity, which creates a low-pressure zone in the throat and withdraws secondary fluid. Finally, the high-pressure primary fluid mixes with low-pressure secondary fluid at the throat and diffuses to the outlet via a diffuser [5]. The drawbacks of the jet pump are friction loss, mixing loss, and the possibility of cavitation. Generally, two types of jet pump are available in the market, central jet pump (CJP) and annular jet pump (AJP) [6]. The nozzle position distinguishes between CJPs and AJPs. In CJPs, the primary pressurized fluid passes through the central nozzle, whereas in AJPs, the pressurized fluid passes through the annular nozzle. Numerous studies [7–9] were conducted on the design and operation of CJPs. Hatzlavramidis [7] proposed the design methodology to model CJPs.

The CJP performance is dependent on the nozzle shape, size, and number [8]. Zhu et al. [9] established the computational methodology for the design and engineering practice of CJPs.

Hence, an AJP is selected to improve the suction performance for the transfer of sensitive goods. Shimizu et al. [10] conducted the experimental analysis on various AJP geometry configurations to evaluate hydraulic and suction performance. Elger et al. [6] introduced dimensionless parameters to study the recirculation flow in an AJP. AJP performance is directly related to the nozzle shape and size [11]. Kwon et al. [12] conducted numerical analysis on an AJP and showed that recirculation mainly occurs under partial flow conditions. Numerical analysis showed that AJPs are more efficient in transportation [13].

The screw centrifugal pump (SCP) is used for slurries, sewage, and sensitive goods transfer. The SCP has a large and open channel from suction to discharge, which helps to transfer the solid particles without clogging. SCPs have a three-dimensional spiral blade added to the conical hub cone. It is the combination of screw pump and centrifugal pump which provides spiral propeller and centrifugal effects, respectively [14]. The higher efficiency, no blockage area, a wide range of operation, and better solid handling capability are the advantages of screw centrifugal pumps over traditional slurry pumps [15]. Few studies were conducted to understand the SCP. The meridional shape parameters of the screw centrifugal pump influence the performance and internal flow [16]. The axial thrust becomes larger where the impeller radius reaches the tongue of the volute casing [17]. Cheng et al. [18] explained the parametric equation for the design of the SCP impeller blade. Guo et al. [19] showed the design method and internal flow behavior of the SCP.

The cavitation occurrence is the main problem for the proper operation of the AJP and the SCP. Cavitation vapor bubbles occur in the nozzle of the AJP and inlet of the SCP impeller blade when they operate below the saturated vapor pressure. The cavitation reduces the pump efficiency and damages the transported goods. The instability of the re-entrant jet and pressure gradient in the re-entrant jet creates cloud cavitation in the divergence section of the AJP [20]. Xiao et al. [21] conducted cavitation analysis in the AJP. Cavitation in the AJP can be caused by increasing the primary jet velocity or decreasing pump outlet pressure [22]. The cavitation phenomenon in the SCP is like in the centrifugal pump and is caused by reducing the inlet pressure. Backflow vortex cavitation and tip leakage cavitation occur at the impeller inlet of the SCP. Cavitation in the AJP and SCP is dependent on the flow condition. Cavitation causes severe damage to sensitive goods such as fish [23]. The improvement of pressure distribution will suppress cavitation in the AJP and the SCP.

The flow field in the AJP and SCP models are alike as a diffuser without and with an impeller, respectively. The diffuser is a pressure-momentum device that focuses on recovering static pressure at the expense of kinetic energy [24]. The static pressure recovery coefficient for the diffuser is calculated as

$$C_{PR} = \frac{p_2 - p_1}{q_1} \quad (1)$$

$$q_1 = 0.5\rho v_1^2 \quad (2)$$

where p is static pressure (Pa), q is dynamic pressure (Pa), v is velocity (m/s), ρ is the density of fluid (kg/m^3), C_{PR} is the pressure recovery coefficient, and subscripts 1 and 2 represent the inlet and outlet of the diffuser.

J-Groove is a simple passive approach to suppress cavitation in the diffuser of AJP and the impeller wall of the SCP [25,26]. It induces the reverse jet flow and suppresses cavitation in the diffuser wall [27]. The main design parameters for J-Groove are depth, length, angle, and number [28], and its depth plays a vital role in the reverse flow rate and suction performance improvement [29].

The flow in J-Groove is dependent on the pressure difference. In a diffuser $p_2 > p_1$, it directs the flow in the J-Groove from the outlet to the inlet of the diffuser. Hence, a reverse flow can be observed in the diffuser with J-Groove. This study is focused on the reverse

flow rate influence on the hydraulic and suction performance of AJP and SCP models. The study objective is to estimate the reverse flow rate through J-Groove passages in AJP and SCP models. Figure 1 shows a flow chart that evaluates the reverse flow rate in AJP and SCP models.

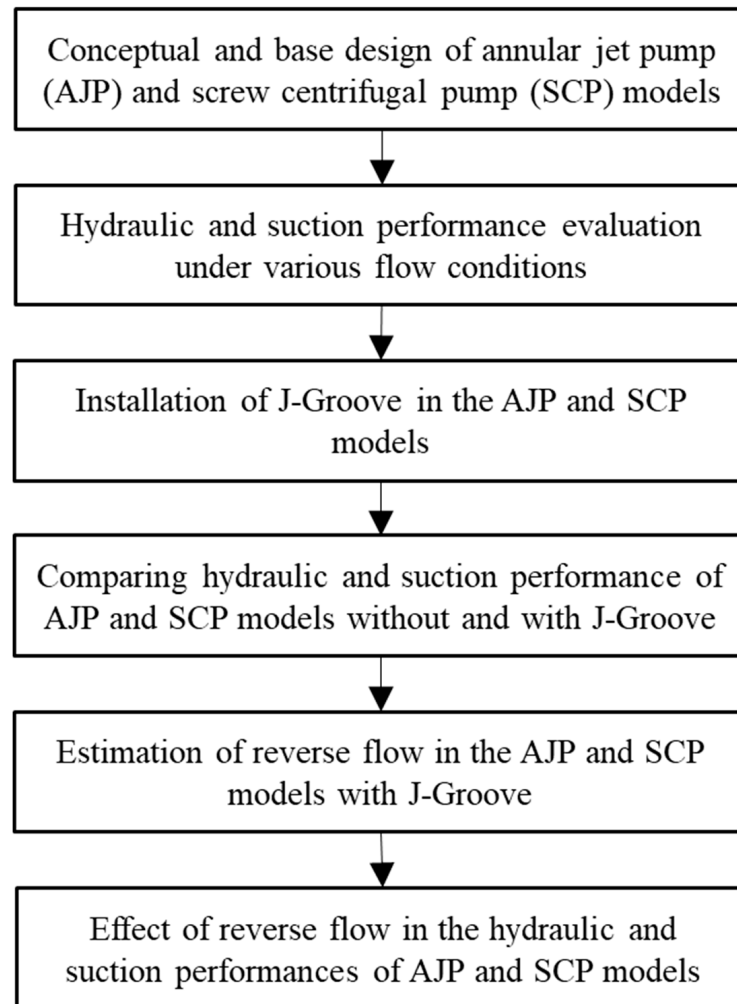


Figure 1. Workflow process for the estimation of reverse flow in AJP and SCP models with J-Groove.

2. Test Pump Models and J-Groove Shape Configuration

2.1. Annular Jet Pump Model

The conceptual design of the AJP model was adopted from the previous studies [23,28]. The 3D and schematic diagrams of the AJP model are shown in Figure 2. The nozzle, throat, and diffuser are essential components of the AJP model. The design parameters of the AJP model are indicated in Table 1 [29]. The area ratio and diffuser angle are considered crucial parameters for the design of the AJP model. The area ratio is defined as in Equation (3).

$$m = \frac{A_t}{A_j} \quad (3)$$

$$A_t = \frac{\pi}{4} D_t^2 \quad (4)$$

$$A_j = \frac{\pi}{4} (D_a^2 - D_s^2) \quad (5)$$

where m is the area ratio, A_t is the area of the throat, and A_j is the area of the jet.

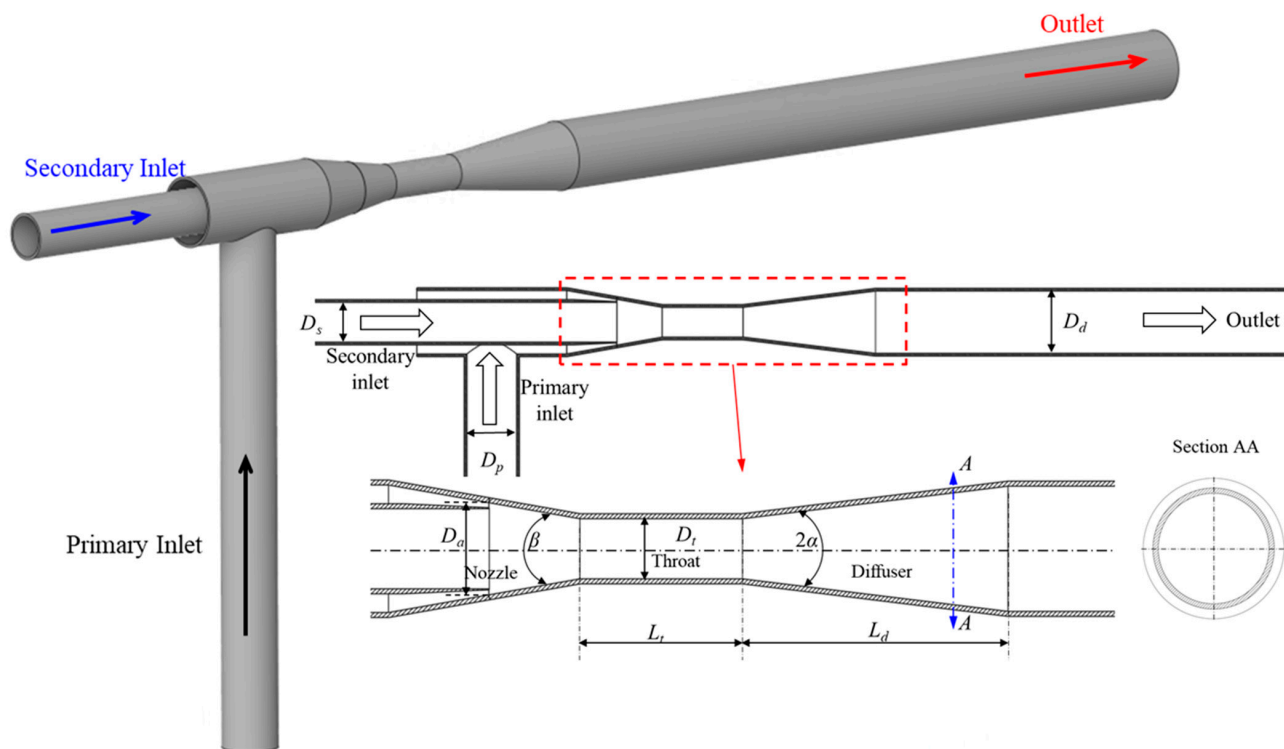


Figure 2. Three-dimensional and schematic views of annular jet pump (AJP) model.

Table 1. Specification of annular jet pump model [29].

Nomenclature	Size Ratio	Values
Outlet pipe diameter, D_d	D_d/D_t	2.08
Primary pipe diameter, D_p	D_p/D_t	1.67
Secondary pipe diameter, D_s	D_s/D_t	1.33
Nozzle diameter, D_a	D_a/D_t	1.53
Throat diameter, D_t		1.00
Diffuser length, L_d	L_d/D_t	8.33
Throat length, L_t	L_t/D_t	2.7
Diffuser angle, α		3.5°
Nozzle angle, β		20.0°
Area ratio, m		1.75

2.2. Screw Centrifugal Pump Model

The screw centrifugal pump conceptual design was adopted from a previous study [30]. Figure 3a,b show the 3D and meridional shapes of the SCP model, respectively. The specific speed was used to categorize the screw centrifugal pump. The design parameters of the screw centrifugal pump model are indicated in Table 2.

$$n_{sp} = \frac{3.65n\sqrt{Q}}{H} \tag{6}$$

where n_{sp} is the specific speed, n is the rotation speed (650 min^{-1}), Q is the design flow rate ($0.064 \text{ m}^3/\text{s}$), and H is the total head of SCP (4 m).

Table 2. Specification of screw centrifugal pump model [30].

Nomenclature	Size Ratio	Value
Total radial diameter, D_{2max}	D_{2max}/D_e	1.39
Hub radial diameter, D_{2min}	D_{2min}/D_e	1.30

Table 2. Cont.

Nomenclature	Size Ratio	Value
Entrance pipe diameter, D_e		1.00
Discharge length, B	B/D_e	0.46
Total axial length, L	L/D_e	1.46
Hub axial length, L_2	L_2/D_e	1.09
Length between a_2b_4 , L_3	L_3/D_e	0.61
Length between b_2b_4 , L_4	L_4/D_e	0.35
Length between b_3b_4 , L_5	L_5/D_e	0.13
Length between a_4b_4 , B_c	B_c/D_e	0.30
Inclination angle 1, α_1		30.0°
Inclination angle 2, α_2		41.2°
Inlet angle, α_0		39.9°
Outlet angle, α_3		10.0°

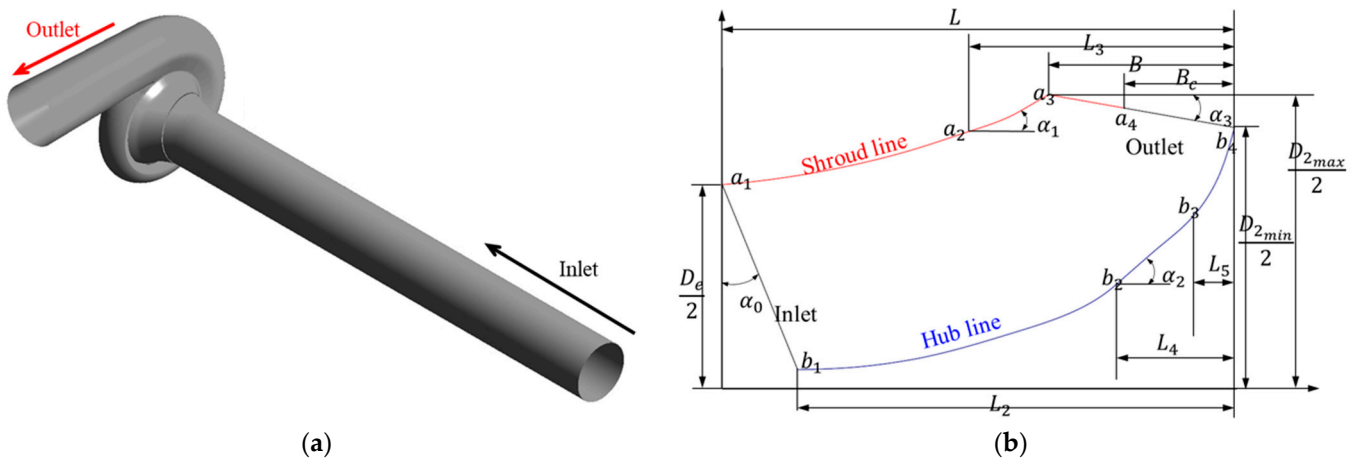


Figure 3. (a) Three-dimensional view and (b) meridional shape of screw centrifugal pump (SCP) model.

2.3. J-Groove Shape Parameters for AJP and SCP Models

The J-Groove is engraved in the diffuser wall or inlet pipe to suppress cavitation in the pump. The designs of J-Groove for the AJP and the SCP models are shown in Figures 4 and 5, respectively. The main design parameters of J-Groove are depth (d_{JG}), length (l_{JG}), angle (θ_{JG}), and number (n_{JG}). J-Groove depth is calculated as in Equation (7).

$$d_{JG} = r_2 - r_1 \tag{7}$$

where r_2 and r_1 are the outer and inner radii of J-Groove.

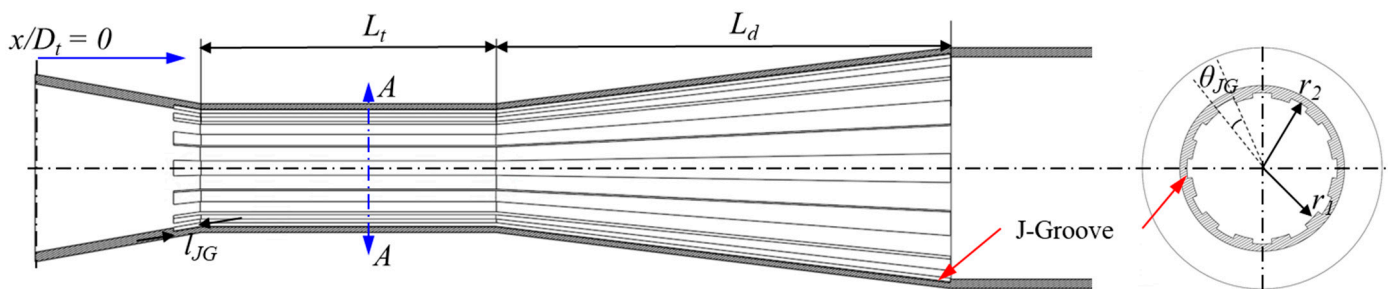


Figure 4. Schematic view of J-Groove shape parameters in annular jet pump model.

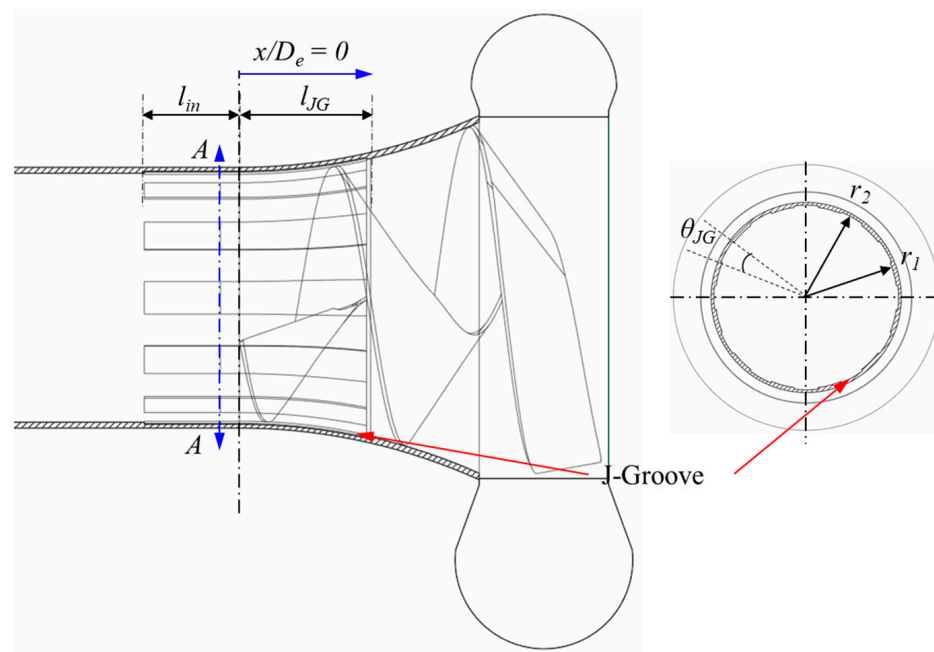


Figure 5. Schematic view of J-Groove shape parameters in screw centrifugal pump model.

The angle (θ_{JG}) and number (n_{JG}) contribute to the width and the surface area of the J-Groove passage. It is attached to the nozzle, throat, and diffuser in the AJP model with constant length in the throat and the diffuser of the AJP model. Similarly, J-Groove is attached to the impeller and inlet pipe walls in the SCP model with a length (l_{in}) of 500 mm in the inlet pipe. The initial J-Groove design shape is shown in Table 3.

Table 3. Shape parameters of J-Groove for AJP and SCP models.

Nomenclature	J-Groove in AJP Model		J-Groove in SCP Model	
	Size Ratio	Value	Size Ratio	Value
Depth, d_{JG}	d_{JG}/D_t	0.06	d_{JG}/D_e	0.01
Length, l_{JG}	l_{JG}/D_t	0.32	l_{JG}/D_e	0.44
Angle, θ_{JG}		12°		12°
Number, n_{JG}		15		15

2.4. Numerical Methodology

ANSYS CFX 19.2 [31] was used to perform CFD analysis, and the numerical grids were generated using ANSYS ICEM 19.2 [31]. The flow in the AJP model is steady and incompressible because it does not have any moving parts. The structured grids of the primary inlet, secondary inlet, nozzle, and diffuser of the AJP model were used for the proper CFD analysis. Figure 6 shows hexahedral grids of the inlet pipes, nozzle, and diffuser of the AJP model. The volute and the impeller structured mesh of the SCP model are shown in Figure 7. The y^+ value near the wall of the primary inlet, secondary inlet, nozzle, diffuser, and outlet pipe of the AJP model are 3.54, 0.33, 2.75, 0.73, and 0.14, respectively. However, the impeller of the SCP model is a complex structure compared to the AJP model. The y^+ value near the impeller wall of the SCP model is 60.

The Reynolds-averaged Navier–Stokes (RANS) equations were used to compute the steady-state analysis in AJP and SCP models. The root mean square residuals of the RANS equation for mass and momentum is maintained as lower than 10^{-5} . The realizable κ - ϵ and shear stress turbulence models were selected to simulate the flow behavior in the AJP and SCP models, respectively. The realizable κ - ϵ turbulence model was used to evaluate the flow prediction for the spreading of jets. The realizable κ - ϵ model could calculate the viscous sub-layer near the wall for $y^+ \leq 5$ [28]. Therefore, the numerical grids for the

AJP model components have a y^+ value of less than 5. The shear stress transport (SST) model was adopted to conduct the CFD analysis in the SCP model. The SST model was designed to predict accurate flow using automatic near-wall treatment. The $1 < y^+ < 100$ range grids were suitable for the SST model with automatic near-wall treatment. The SST model was appropriate for the flow prediction in high rotation speed and strong separate flow. Hence, the y^+ value for the SCP model is less than 100, which is desirable for the SST model application.

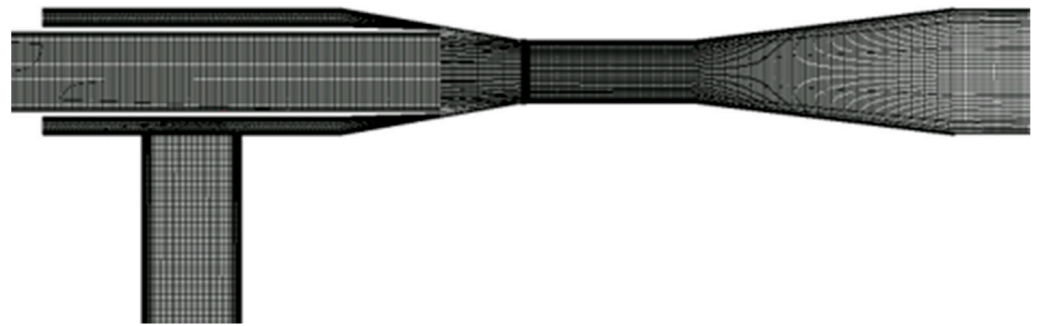


Figure 6. Numerical grids of annular jet pump model.

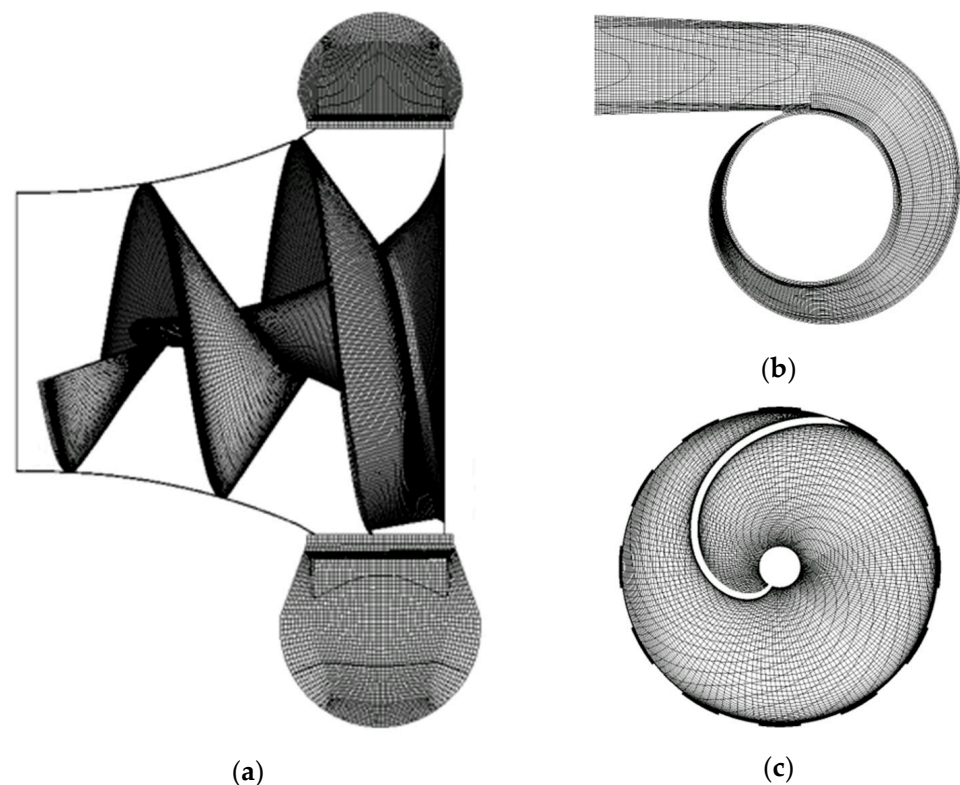


Figure 7. Numerical grids of (a) impeller of SCP, (b) volute, and (c) cross-section view of impeller with J-Groove.

The mesh dependency test was conducted to select the optimum mesh number for the stable CFD analysis using the grid convergence index (GCI) test [32]. Table 4 and Figure 8 show the mesh dependency test results for the AJP model. The mesh dependency test concluded that 4.2 million nodes for AJP models were selected because the grid convergence index is less than 5% with stable CFD analysis results. The grid dependency test for the SCP model is shown in Table 5 and Figure 9. The deviation in the efficiency is negligible with an increase in the grid numbers. The convergence index is less than 1% for the CFD

analysis of the SCP model. The mesh dependency test indicated 3.6 million nodes for the stable CFD analysis of the SCP model.

Table 4. Grid dependency test for AJP CFD analysis via GCI method.

	$N_1 = 4.1 \times 10^5$ ϕ_1 (Mass Ratio)	$N_2 = 4.2 \times 10^6$ ϕ_2 (Pressure Ratio)	$N_3 = 7.6 \times 10^6$ ϕ_3 (Efficiency)
r_{21}	2.1766	2.1766	2.1766
r_{32}	2.6461	2.6461	2.6461
ϕ_1	0.4486	0.3981	17.8600
ϕ_2	0.4484	0.4246	19.0400
ϕ_3	0.24	0.4118	18.6300
ϵ_{32}	0.0040	-0.0128	-0.4100
ϵ_{21}	-0.0002	0.0265	1.1800
p	0.8352	1.3240	1.4327
ϕ_{ext}^{21}	0.4488	0.3880	17.4707
ϵ_a^{21}	0.847%	3.441%	4.311%
ϵ_{ext}^{21}	0.798%	7.413%	7.790%
GCI_{fine}^{21}	0.044%	3.168%	2.724%

where r is the refinement factor between the coarse and fine grid, ϕ_1 is the mass ratio, ϕ_2 is the pressure ratio, ϕ_3 is efficiency, p is the formal order of accuracy of the algorithm, $\epsilon_{32} = \phi_3 - \phi_2$, $\epsilon_{21} = \phi_2 - \phi_1$, ϵ_a^{21} is the approximate relative error, ϵ_{ext}^{21} is the extrapolated relative error, and GCI_{fine}^{21} is the fine-grid convergence index.

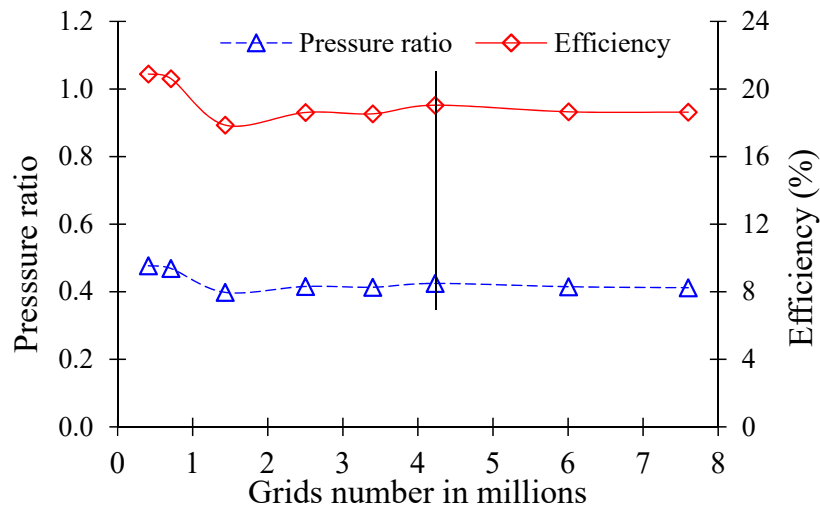


Figure 8. Grid dependency test for AJP model.

Table 5. Grid dependency test for SCP CFD analysis via GCI method.

	$N_1 = 1.9 \times 10^6$ ϕ_1 (Efficiency)	$N_2 = 2.5 \times 10^6$ ϕ_2 (Power)	$N_3 = 3.6 \times 10^6$ ϕ_3 (Head)
r_{21}	1.095	1.095	1.095
r_{32}	1.110	1.110	1.110
ϕ_1	73.414	2.912	2.478
ϕ_2	73.469	2.917	2.471
ϕ_3	72.879	2.876	2.466
ϵ_{32}	-0.589	-0.041	-0.015
ϵ_{21}	0.055	0.005	0.003
p	23.016	20.941	15.305
ϕ_{ext}^{21}	73.489	2.919	2.482
ϵ_a^{21}	0.075%	0.163%	0.128%
ϵ_{ext}^{21}	0.102%	0.217%	0.159%
GCI_{fine}^{21}	0.013%	0.036%	0.053%

where r is the refinement factor between the coarse and fine grid, ϕ_1 is the efficiency, ϕ_2 is power (kW), and ϕ_3 is head (m).

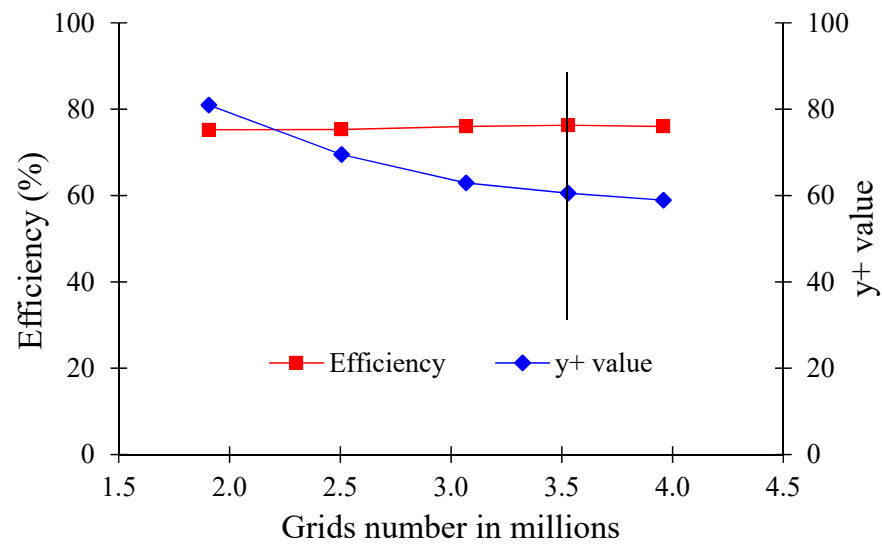


Figure 9. Grid dependency test for SCP model.

The pump efficiency, mass ratio, pressure ratio, and cavitation number were used as performance measurements for the AJP model, which was evaluated using Equations (8)–(11). Equations (12) and (13) were used to calculate the pump efficiency and cavitation number for the SCP model, respectively.

$$q = \frac{Q_s}{Q_n} \quad (8)$$

$$p = \frac{p_m^T - p_s^T}{p_n^T - p_m^T} \quad (9)$$

$$\eta_{AJP} = p \times q \quad (10)$$

$$\sigma_n = \frac{p_n - p_v}{0.5\rho v_n^2} \quad (11)$$

$$\eta_{SCP} = \frac{\tau\omega}{\rho gQH} \quad (12)$$

$$\sigma_s = \frac{p_{in} - p_v}{\rho gH} \quad (13)$$

where q is the mass ratio, p is the pressure ratio, η_{AJP} is the AJP model hydraulic efficiency, Q_s is the secondary flow rate, Q_n is the flow rate at the nozzle exit, p_m^T is the total pressure at the diffuser outlet, p_s^T is the total pressure at the secondary inlet, p_n^T is the total pressure at the nozzle exit, σ_n is the cavitation number for AJP, p_n is the static pressure at the nozzle exit, p_v is the vapor pressure of water at 25 °C, v_n is the velocity at the nozzle exit, ρ is the density of water at 25 °C, η_{scp} is the SCP model's hydraulic efficiency, τ is input torque, ω is the angular velocity of the impeller, g is acceleration due to gravity, Q is flow rate, H is the total head of the SCP, p_{in} is the static pressure at the SCP inlet, and σ_s is the cavitation number for the SCP.

The boundary conditions for the CFD analysis for the AJP and SCP models are shown in Table 6. The inlet boundary conditions were total pressure at the primary inlet and mass flow rate at the secondary inlet of the AJP model. The outlet of the AJP was set as static pressure. The inlet and outlet of the SCP model were mass flow rate and static pressure, respectively. The mass flow rate varied from partial to full load conditions to prepare the performance curves of the SCP model. The suction performance was evaluated using the Rayleigh–Plesset equation [33].

Table 6. Information of boundary conditions for CFD analysis of AJP and SCP models.

Parameter/Boundary	Condition/Value	
	AJP	SCP
Primary Inlet	Total Pressure	Mass Flow Rate
Secondary Inlet	Mass Flow Rate	-
Outlet	Static Pressure	Static Pressure
Turbulence model	Realizable κ - ϵ	SST
Grid interface connection	General Grid Interface (GGI)	General Grid Interface (GGI)
Interface model	Steady State/Frozen rotor	Steady State/Frozen rotor
Walls	No slip wall (roughness: smooth)	No slip wall (roughness: smooth)

3. Results and Discussion

3.1. Pump Performance Curves of AJP and SCP Models

Figure 10 shows the performance curves of the AJP model. The experimental results for the AJP model were adopted from Long et al. [23]. The performance curves for the AJP model were evaluated by varying the mass ratio (q) from 0.1 to 0.8, the best efficiency point at $q = 0.5$. The efficiency difference between experimental data and CFD analysis results is less than 1% at $q = 0.5$. Hence, the experimental and CFD analysis showed good agreement between them. Therefore, the CFD analysis method is acceptable for further analysis. The best efficiencies of the AJP model without and with initial J-Groove are 19.75% and 18.88%, respectively. The installation of the J-Groove has no significant effect on the efficiency drop. It is concluded that the installation of J-Groove shows no adverse influence on the pump performance.

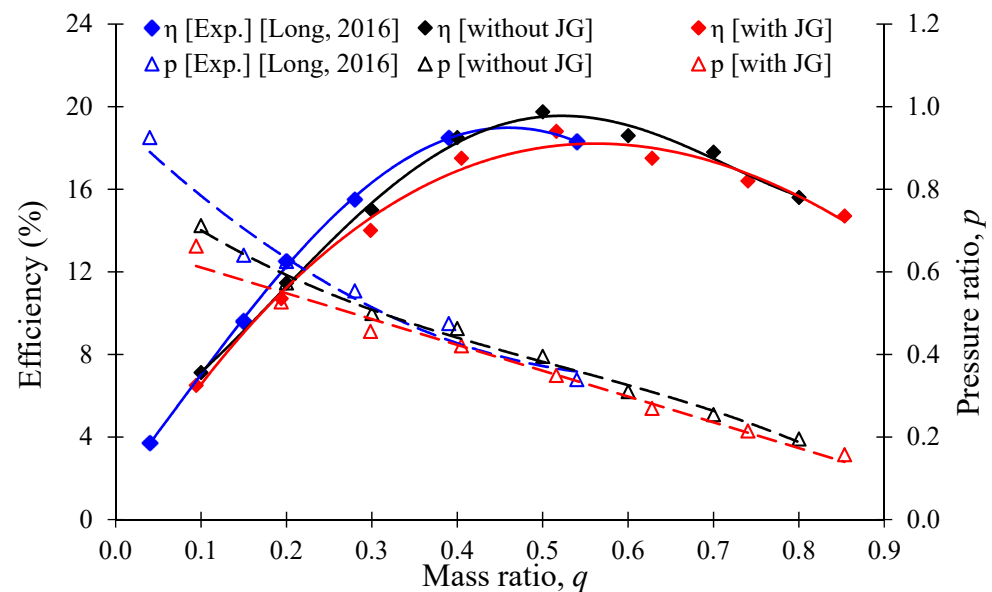
**Figure 10.** Comparison of performance curves between experimental [23] and CFD analysis of AJP model without and with J-Groove (JG).

Figure 11 shows the performance curves for the SCP model. The best efficiency point for the SCP model matches the design point. It is concluded that the design method of the SCP model is acceptable. The best efficiencies of the SCP model are 76.54% and 71.42% without and with initial J-Groove, respectively. This showed that the installation of J-Groove has a slightly negative effect on the SCP model performance.

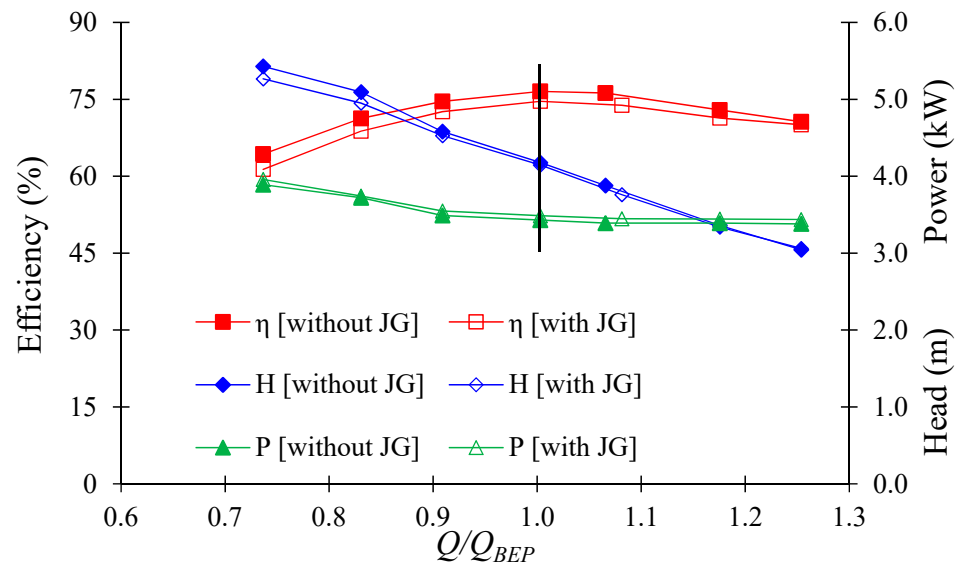


Figure 11. Performance curves comparison without and with J-Groove in SCP model.

3.2. Suction Performance Curves of AJP and SCP Models

J-Groove installation improved the pressure distribution in the AJP and SCP models. The pressure distribution in the AJP model at $q = 0.4, 0.5,$ and 0.6 is shown in Figure 12. The minimum pressures at the throat of the AJP model without J-Groove are 82 kPa, 62 kPa, and 44 kPa at $q = 0.4, 0.5,$ and 0.6 , respectively. The J-Groove passage transfers the high-pressure fluid from the diffuser to the throat and reduces the pressure at the diffuser outlet. The J-Groove installation in the AJP model increases the minimum pressure at the throat by 22%, 23%, and 40% at $q = 0.4, 0.5,$ and 0.6 , respectively. The pressure improvement plays a vital role in cavitation suppression in the AJP model. Hence, the possibility of cavitation in the AJP model is reduced significantly.

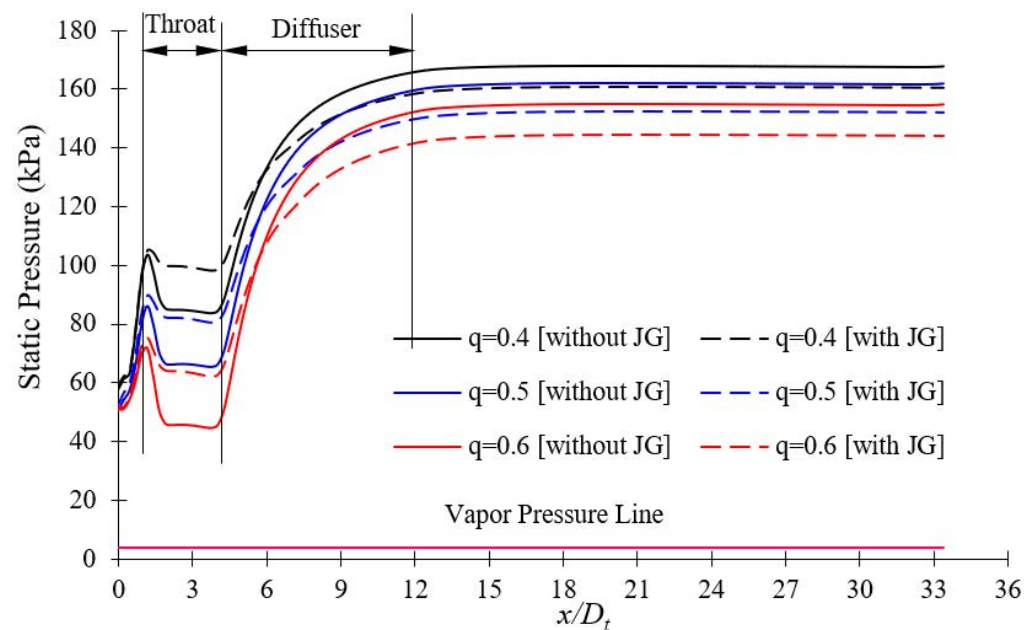


Figure 12. Pressure distribution comparison in the AJP model without and with J-Groove.

Figure 13 shows the pressure distribution in the SCP model. At the inlet of the impeller, the pressure is relatively lower than in other locations. The installation of J-Groove improves the pressure distribution at the impeller inlet in the SCP model by transferring high-pressure fluid from the impeller outlet to the impeller inlet. At $x/D_e = 0$, the static

pressure is improved in the SCP model with J-Groove. The J-Groove installation in the SCP model increases the minimum pressure at the impeller inlet by 1.1%, 1.4%, and 1.9% at $Q/Q_{BEP} = 0.75, 1.00,$ and $1.15,$ respectively. It is conjectured that the reverse flow from the J-Groove passage increases the pressure at the impeller inlet and decreases the possibility of cavitation in the SCP model.

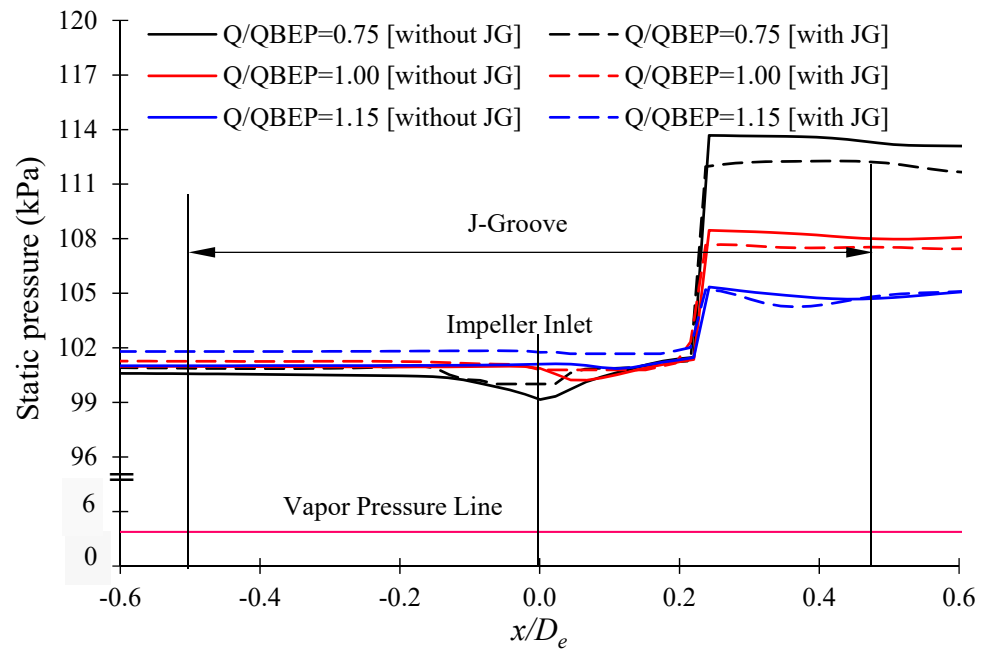


Figure 13. Pressure distribution comparison in the SCP model without and with J-Groove.

The suction performance of the AJP model without and with initial J-Groove is shown in Figure 14. The suction performance is directly affected by the pressure distribution. The critical cavitation numbers are 0.19, 0.30 and 0.38 at $q = 0.4, 0.5$ and $0.6,$ respectively. The installation of J-Groove improves the suction performance in the AJP model. The critical cavitation number is improved from 0.38 to 0.30, 0.30 to 0.24 and 0.19 to 0.18 at $q = 0.6, 0.5$ and $0.4,$ respectively. Hence, the installation of J-Groove drastically improves the suction performance of the AJP model.

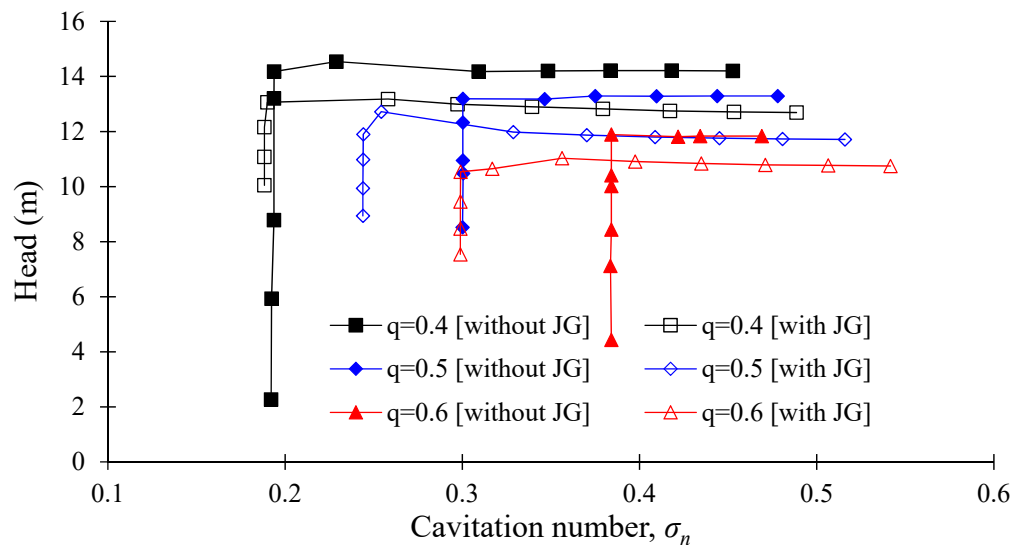


Figure 14. Suction performance comparison in the AJP model without and with J-Groove.

The suction performance of the SCP model without and with initial J-Groove is shown in Figure 15. The installation of J-Groove in the SCP model is an effective method to improve the suction performance. The critical cavitation number is improved from 0.08 to 0.05 and 0.12 to 0.09 at $Q/Q_{BEP} = 0.75$ and 1.00, respectively. Furthermore, the significant improvement at $Q/Q_{BEP} = 1.15$ is indicated in Figure 15. The critical cavitation number is improved from 0.36 to 0.18 at $Q/Q_{BEP} < 1.15$. Hence, the suction of the SCP model is improved considerably with the installation of J-Groove.

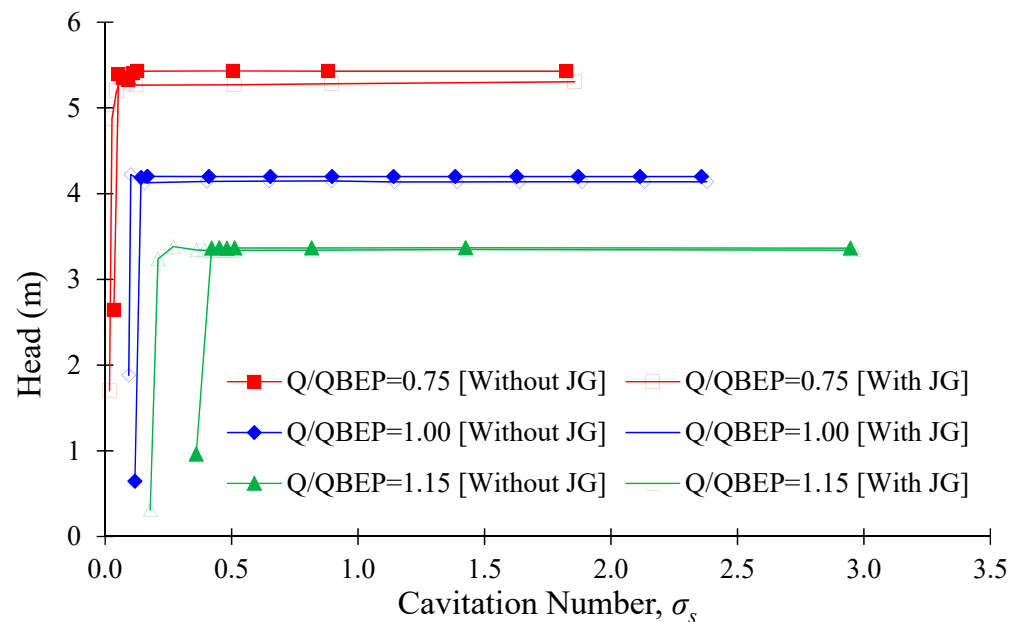


Figure 15. Suction performance comparison in the SCP model without and with J-Groove.

3.3. Estimation of Reverse Flow Rate by J-Groove Installation

The working mechanism of J-Groove is transferring the jet flow from the high-pressure region to the low-pressure region via groove passage [27]. The jet flow helps to increase the pressure in the low-pressure region. The reverse jet flow is dependent on the pressure difference. The reverse flow rate ratio is the mass flow rate transfer from the J-Groove passage to the best efficiency flow rate for the AJP and SCP models, respectively. The reverse flow rate ratio is used to evaluate the flow mechanism in the J-Groove. The reverse flow rate ratio is calculated using Equation (12).

$$q_{rf} = \frac{q_{JG}}{Q_{BEP}} \quad (14)$$

Where q_{rf} is the reverse flow rate ratio, q_{JG} is the reverse mass flow rate through J-Groove (kg/s), and Q_{BEP} is the mass flow rate of AJP or SCP model at the BEP.

The reverse flow rate ratio and pressure difference variation in the J-Groove passage of AJP and SCP is shown in Figure 16, and d represents the size ratio of J-Groove depth. In the AJP model, the reverse flow rate ratio increases with an increase in the flow rate. However, in the SCP model, the reverse flow rate ratio decreases with an increase in the flow rate. The variation in reverse flow rate ratio and pressure difference with J-Groove depth in AJP and SCP models is shown in Figure 16. The variation in pressure distribution causes the difference in the reverse flow rate ratio at various flow rates. The pressure difference between the J-Groove inlet and outlet is higher in the high load condition than in the partial load condition in the AJP model. Similarly, the pressure difference is higher in the partial load condition than in the high load condition in the SCP model. Therefore, the reverse flow behavior is contradictory between the AJP and SCP models.

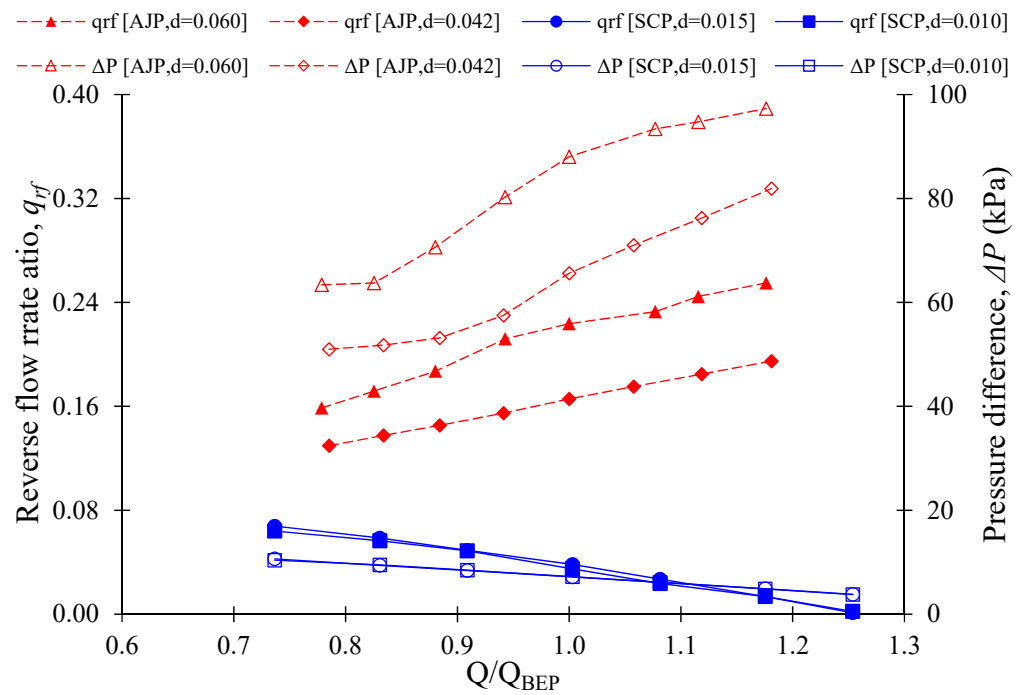


Figure 16. Reverse flow rate ratio and pressure difference variation in the J-Groove channel of AJP and SCP models.

The pressure contours in the AJP model are shown in Figure 17. The absence of moving components is the reason for the smooth pressure distribution in the AJP model. Figure 17 shows the pressure difference between the J-Groove inlet and outlet in the AJP model. The velocity vector in the AJP model with J-Groove is shown in Figure 18. The velocity vector in the J-Groove passage is in the opposite direction to the main flow. The velocity vectors show that the installation of J-Groove improves the pressure distribution by reverse jet flow. It is concluded that the J-Groove induces the reverse jet flow, which improves suction performance.

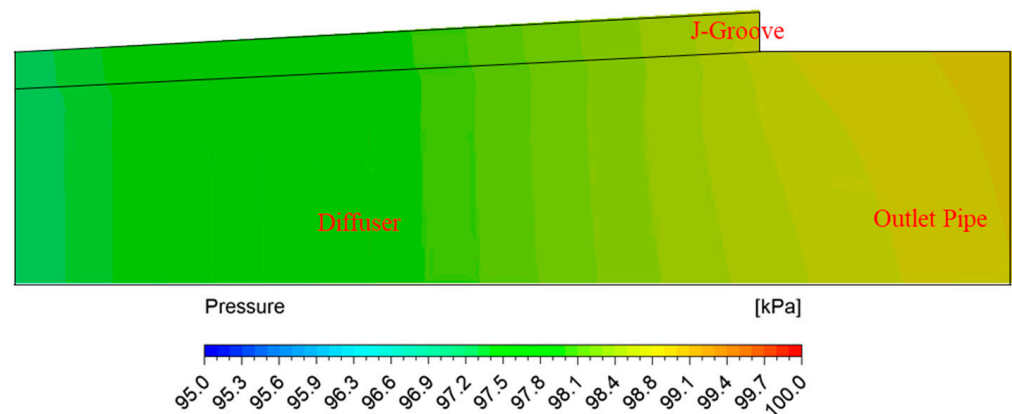


Figure 17. Pressure contours in the AJP model with J-Groove at $q = 0.5$.

The pressure contours in the SCP model are shown in Figure 19. The pressure is increased considerably via the impeller. A clear difference in the pressure distribution is observed in the SCP model. The rotation of the impeller increases the pressure drastically in the SCP model. Figure 20 shows the velocity vectors in the SCP model with J-Groove. The velocity vector clarifies the reverse jet flow occurrence in the J-Groove flow passage, the direction of which is opposite to the main flow. The pressure difference between the J-Groove inlet and outlet induces the reverse flow in the AJP and SCP models.

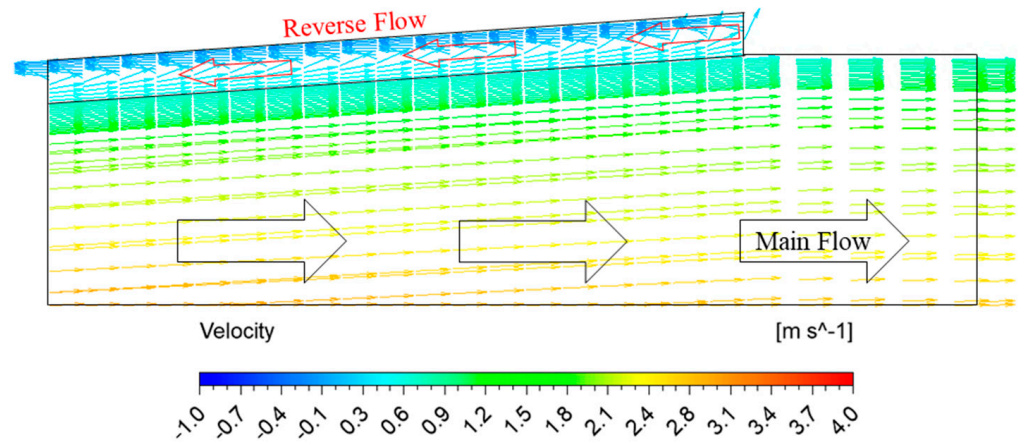


Figure 18. Velocity vectors in the AJP model with J-Groove at $q = 0.5$.

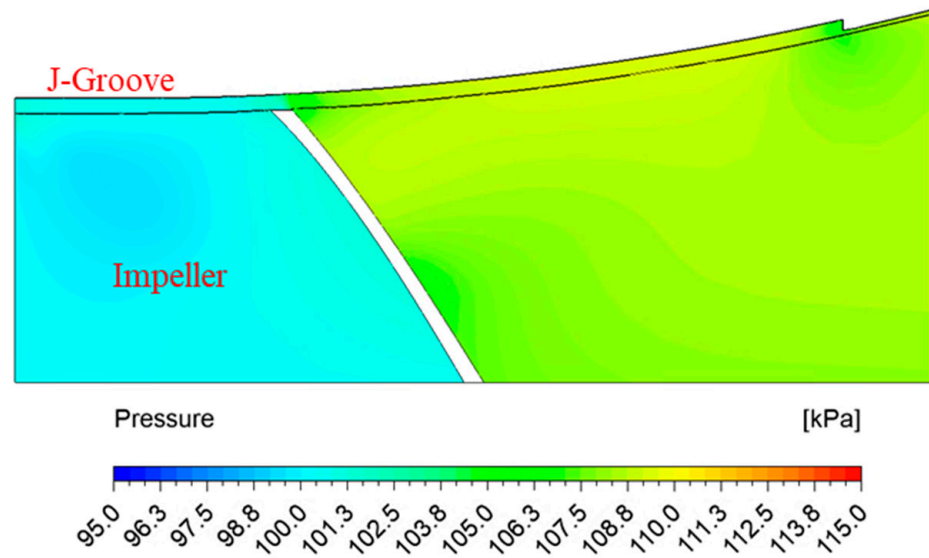


Figure 19. Pressure contours in the SCP model with J-Groove at $Q/Q_{BEP} = 1.00$.

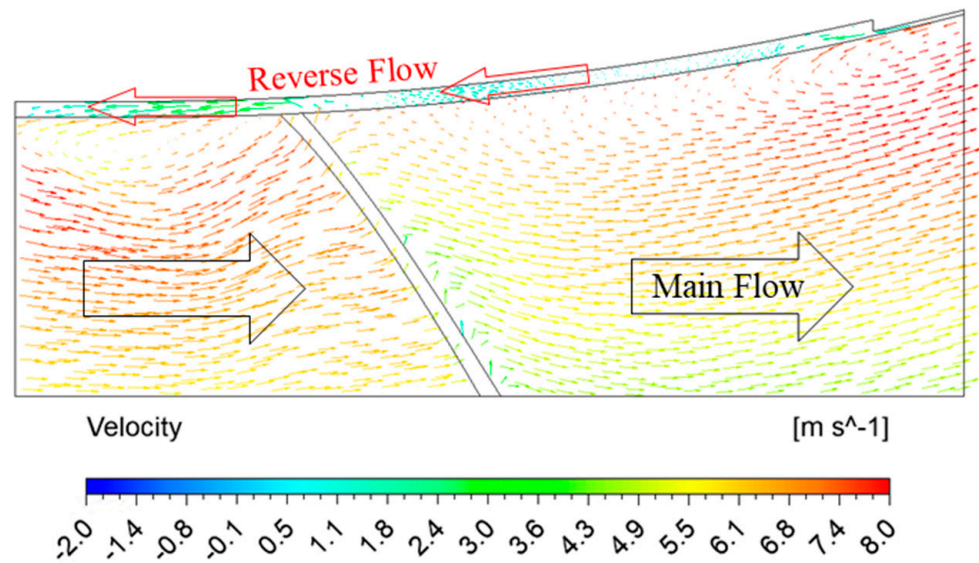


Figure 20. Velocity vector distribution in the SCP model with J-Groove at $Q/Q_{BEP} = 1.00$.

3.4. Relationship between Reverse Flow Rate in J-Groove Channel and Pump Performance

The comparison of the performance curves and reverse flow rate ratio in the AJP model is shown in Figure 21. The reverse flow rate ratio varies from 0.16 to 0.26 in the AJP model. The pump efficiency decreases with an increase in the reverse flow rate ratio. When the reverse flow rate ratio is 0.16 and 0.25, the efficiency is reduced by 0.61% and 0.93%, respectively. The efficiency drop in the AJP model is below 1%, which is insignificant. Figure 22 shows the relation between the reverse flow rate ratio and efficiency drop in the SCP model. In the SCP model, the reverse flow rate ratio is comparatively lower than the AJP model because the design flow rate for the SCP model is higher than the AJP model. When $q_{rf} = 0.064$ and 0.014, the efficiency drops by 2.97% and 1.58% in the SCP model, respectively. The reverse flow rate ratio has a higher efficiency drop in the SCP model than in the AJP model. Hence, the reverse flow rate ratio increases the static pressure at the expense of efficiency drop.

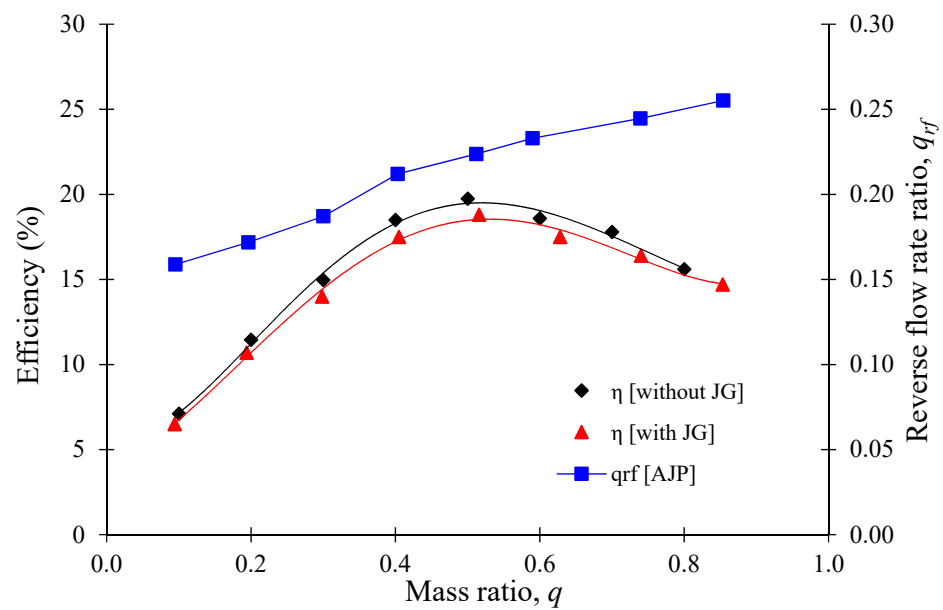


Figure 21. Performance curves of AJP model with reverse flow rate ratio.

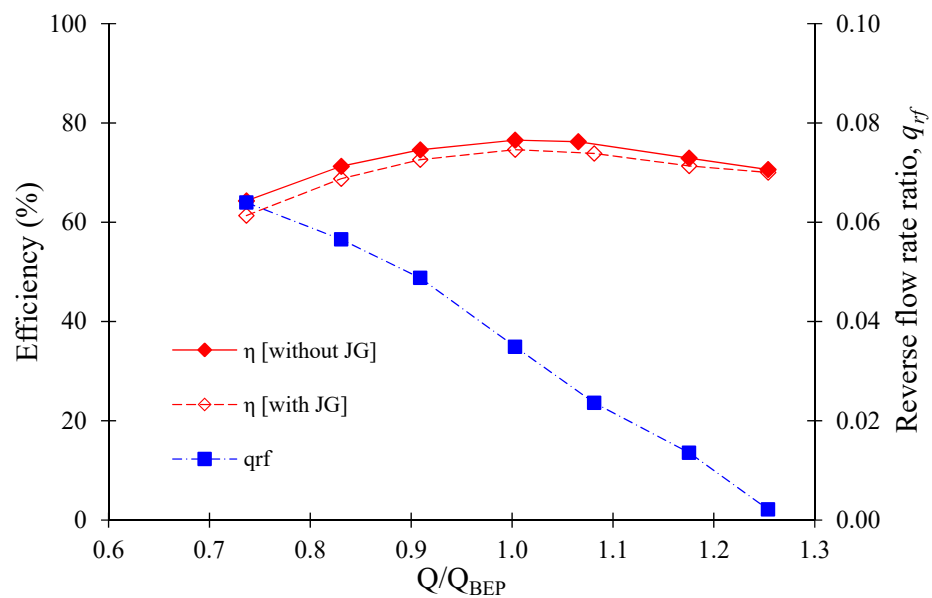


Figure 22. Performance curves of SCP model with reverse flow ratio.

3.5. Relationship between Reverse Flow Rate in J-Groove Channel and Suction Performance

The suction performance and reverse flow rate ratio in the AJP model are shown in Figure 23. The reverse jet flow is dependent on the mass ratio and cavitation number. The reverse flow rate ratio increases with an increase in mass ratio. The reverse flow rate ratio is reduced drastically at the critical cavitation number. When the critical cavitation number is reached, the cavitation clouds are formed at the throat and diffuser of the AJP model and obstruct the reverse flow. At $\sigma_n = 0.36$, the reverse flow rate ratios are 0.14, 0.16, and 0.17 for $q = 0.4, 0.5$, and 0.6 , respectively. The reverse flow rate ratio indicates the occurrence of a critical cavitation number. Figure 23 shows the gradual decrease in the reverse flow rate ratio when the cavitation number (σ_n) approaches the critical value. The reverse flow rate ratio plays an important role in cavitation prediction in the AJP model.

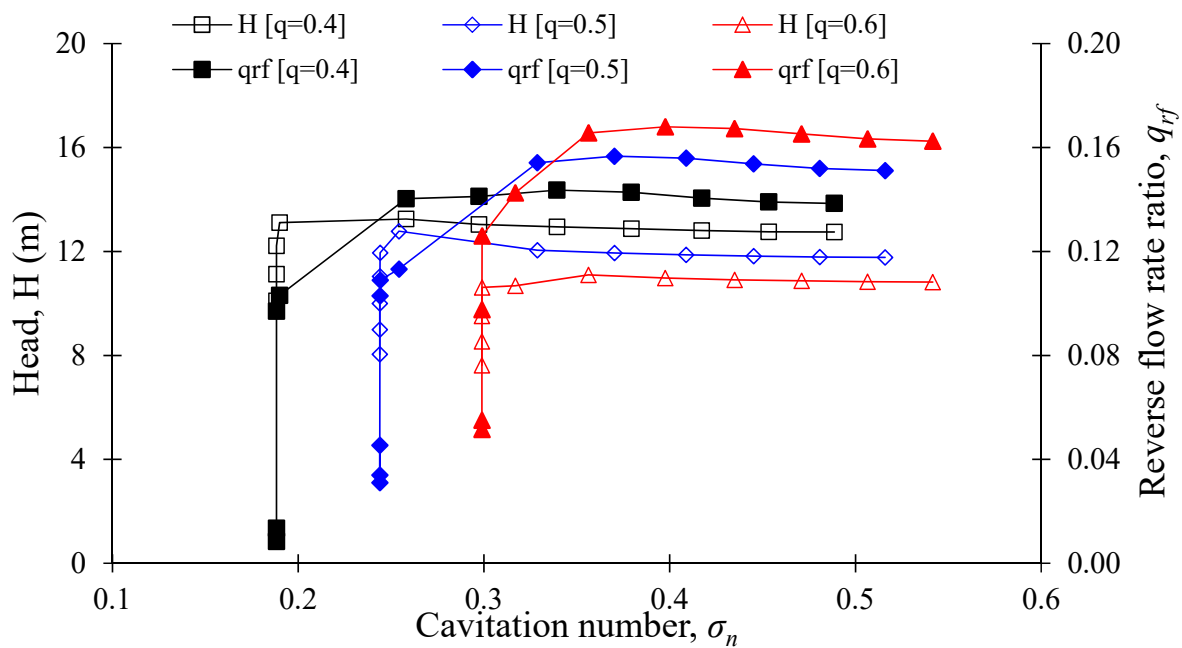


Figure 23. Relationship between suction performance and reverse flow rate in the AJP model with J-Groove.

Figure 24 shows the relation between suction performance and reverse flow rate ratio in the SCP model. The reverse flow rate ratio decreases with an increase in flow rate. At $\sigma_s = 0.5$, the reverse flow rate ratios are 0.09, 0.03, and 0.01 for $Q/Q_{BEP} = 0.75$ and 1.00 and 1.15, respectively. The reverse flow rate ratio decreases drastically with an increase in flow rate in the SCP model. The reverse flow rate ratio tends to decrease gradually when the cavitation number approaches the critical cavitation number. This indicates that the cavitation will initiate with a gradual decrease in the reverse flow rate ratio. The cavitation possibility increases with a decrease in the reverse flow rate ratio in the AJP and SCP models. Figures 23 and 24 confirm that the reverse flow rate ratio tendency with cavitation number is similar in the AJP and SCP models. The reverse flow rate ratio (q_{rf}) can predict the cavitation inception and avoid severe damage to the AJP and SCP models.

3.6. Mechanism of Reverse Flow Rate in AJP and SCP Models

The J-Groove installation induces the reverse flow in the AJP and SCP models. In the AJP model, the fluid flows from the inlet to the outlet via the venturi effect [34]. The continuous primary flow passes through the throat at high velocity from the booster pump. The air is removed from the nozzle, creating a vacuum, and secondary flow is sucked up due to the atmospheric pressure. Finally, the secondary flow is mixed with the high-velocity primary flow at the throat, and the mixed flow passes through a diffuser which gradually reduces the velocity. The J-Groove installation creates the simple narrow flow passages in

the wall of the AJP model. The flow behavior in the J-Groove is dependent on the pressure difference. CFD analysis indicated that the pressure at the J-Groove outlet is higher than the J-Groove inlet, which is in the reverse direction to the main flow. Figure 25 elaborates the flow mechanism of the J-Groove in the AJP model.

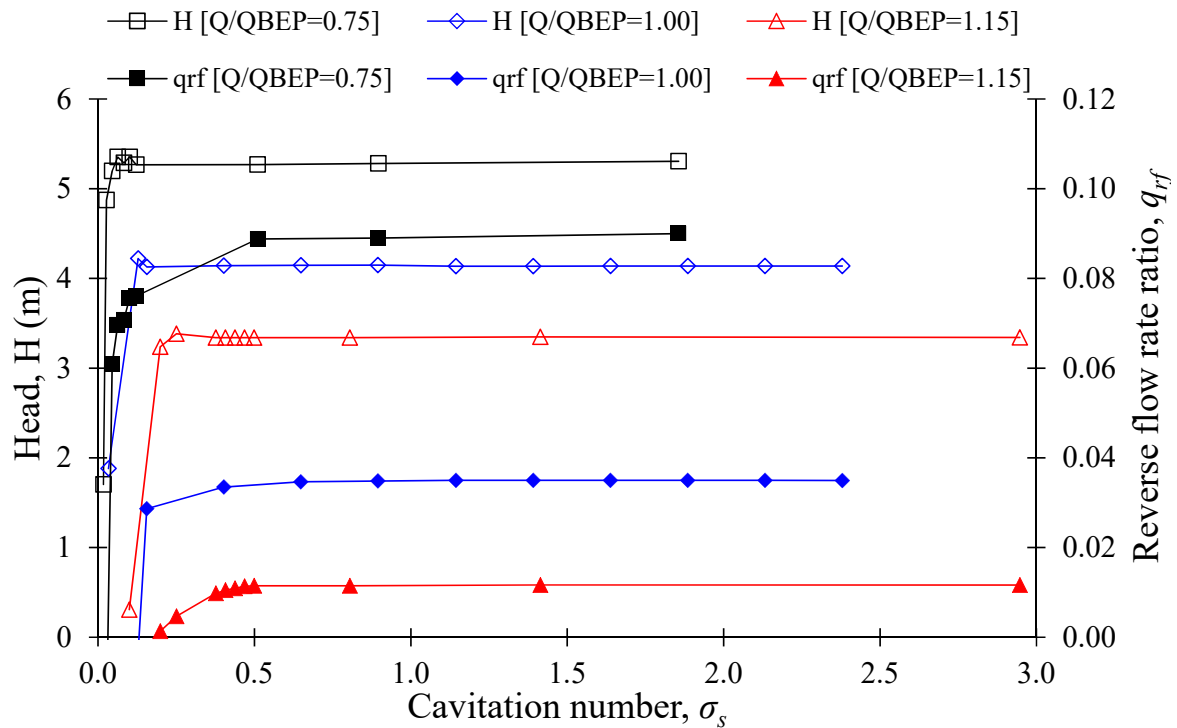


Figure 24. Relationship between suction performance and reverse flow rate ratio in the SCP model with J-Groove.

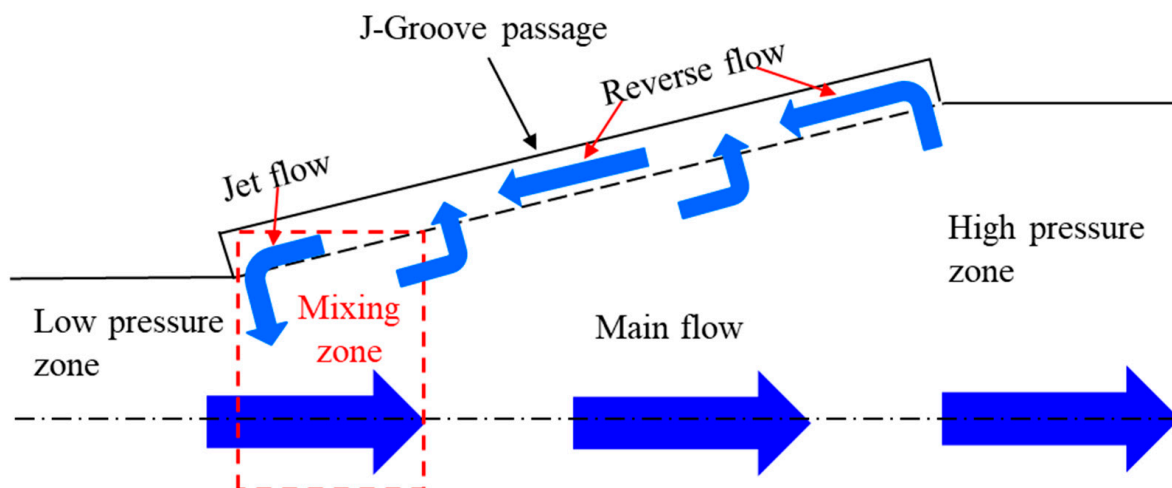


Figure 25. Mechanism of reverse flow in AJP model with J-Groove.

In the SCP, the flow behavior is like an inducer. The impeller rotation transfers flow from a low-pressure inlet to a high-pressure outlet. The installation of J-Groove in the SCP induces reverse flow through the groove channels due to the pressure difference. Therefore, the J-Groove passage transfers flow from the outlet to the inlet of the diffuser casing. The J-Groove flow mechanism in the SCP model is shown in Figure 26.

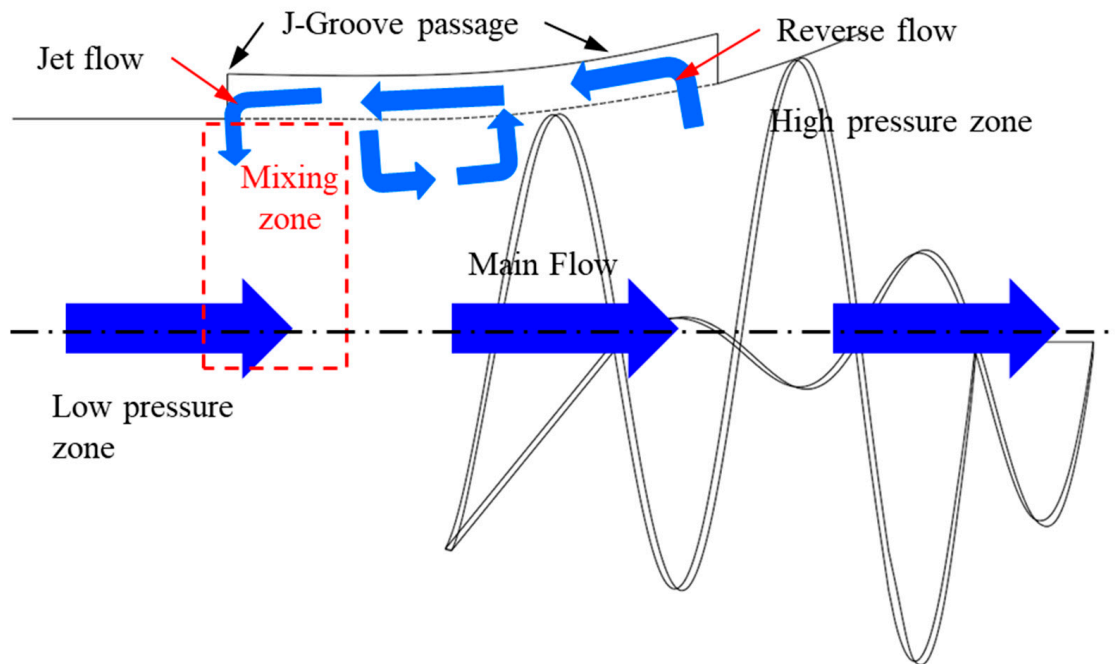


Figure 26. Mechanism of reverse flow in SCP model with J-Groove.

4. Conclusions

The CFD analysis showed that the J-Groove installation in the AJP and SCP models improves the suction performance. The pressure distribution and suction performance of AJP and SCP models are improved drastically with J-Groove installation. The reverse flow rate plays a significant role in suction performance improvement. The pressure distribution in the AJP and SCP models is different because of the impeller. In the AJP model, the reverse flow rate ratio increases with an increase in flow rate. However, the reverse flow rate ratio decreases with an increase in flow rate in the SCP model. The installation of the impeller has a significant impact on the reverse flow rate in the diffuser. In the AJP model, the pressure difference between the inlet and outlet of J-Groove is higher in full load conditions than in partial load conditions. The reverse flow rate is dependent on the pressure difference. In the SCP model, the pressure difference is larger at partial load conditions compared to full load conditions.

The suction performance is directly related to the reverse flow rate ratio. The study concluded that the reverse flow rate ratio is dependent on the pump type, flow rate, and cavitation number. The higher reverse flow rate ratio improves the suction performance in the AJP and SCP models effectively. The reverse flow mechanism in the AJP and SCP models is different. In the AJP model, the simple pressure difference between the inlet and outlet of J-Groove induces the reverse flow. In the SCP model, the rotation of the impeller causes a pressure difference between the suction and pressure side, which contributes to the reverse flow. It is concluded that the J-Groove installation helps to increase the reverse flow rate mainly due to the pressure difference.

Author Contributions: Conceptualization, U.S. and Y.-D.C.; methodology, U.S.; software, Y.-D.C.; validation, U.S. and Y.-D.C.; formal analysis, U.S.; investigation, U.S.; resources, Y.-D.C.; data curation, U.S.; writing—original draft preparation, U.S.; writing—review and editing, U.S. and Y.-D.C.; visualization, U.S.; supervision, Y.-D.C.; project administration, Y.-D.C.; funding acquisition, Y.-D.C. All authors have read and agreed to the published version of the manuscript.

Funding: This research received no external funding.

Conflicts of Interest: The authors declare no conflict of interest.

References

1. Elger, D.F.; Melam, E.T.; Taylor, S.J. A new way to represent jet pump performance. *J. Fluids Eng.* **1991**, *113*, 439–444. [[CrossRef](#)]
2. Deng, X.; Dong, J.; Wang, Z.; Tu, J. Numerical analysis of an annular water-air jet pump with self-induced oscillation mixing chamber. *J. Comput. Multiph. Flows* **2017**, *9*, 47–53. [[CrossRef](#)]
3. Kryzhanivskiy, Y.I. The study on the flow's kinematics in the jet pump's mixing chamber. *Geotech. Min. Mech. Eng. Mach. Build.* **2019**, *1*, 62–68.
4. Kim, Y.K.; Lee, D.Y.; Kim, H.D.; Ahn, J.H.; Kim, K.C. An experimental and numerical study on hydrodynamic characteristics of horizontal annular type water-air ejector. *J. Mech. Sci. Technol.* **2012**, *26*, 2773–2781. [[CrossRef](#)]
5. Nilavalagan, S.; Ravindran, M.; RadhaKrishna, H.C. Analysis of mixing characteristics of flow in a jet pump using a finite-difference method. *Chem. Eng. J.* **1988**, *39*, 97–109. [[CrossRef](#)]
6. Elger, D.F.; Taylor, S.J.; Liou, C.P. Recirculation in an annular-type jet pump. *J. Fluids Eng.* **1994**, *116*, 735–740. [[CrossRef](#)]
7. Hatzlavramidis, D.T. Modeling and design of jet pumps. *SPE Prod. Eng.* **1991**, *6*, 413–419. [[CrossRef](#)]
8. Narabayashi, T.; Yamazaki, Y.; Kobayashi, H.; Shakouchi, T. Flow analysis for single and multi-nozzle jet pump. *JMSE Int. J.* **2006**, *49*, 933–940. [[CrossRef](#)]
9. Zhu, H.; Qiu, B.; Jia, Q.; Yang, X. Simulation analysis of hydraulic jet pump. *Adv. Mater. Res.* **2011**, *204*, 293–296. [[CrossRef](#)]
10. Shimizu, Y.; Nakamura, S.; Kuzuhara, S.; Kurata, S. Studies of the configuration and performance of annular type jet pumps. *J. Fluids Eng.* **1987**, *190*, 205–212. [[CrossRef](#)]
11. Hammoud, A.H. Effect of design and operational parameters on jet pump performance. In Proceedings of the 4th WSEAS International Conference on Fluid Mechanics and Aerodynamics, Elounda, Greece, 21 August 2006.
12. Kwon, O.B.; Kim, M.K.; Kwon, H.C.; Bae, D.S. Two-dimensional numerical simulations on the performance of an annular jet pump. *J. Vis.* **2002**, *5*, 21–28. [[CrossRef](#)]
13. Song, X.G.; Park, J.H.; Kim, S.G.; Park, Y.C. Performance comparison and erosion prediction of jet pumps by using a numerical method. *Math. Comput. Model.* **2013**, *57*, 245–253. [[CrossRef](#)]
14. Guan, X.F. *Modern Pump Theory and Design*; China Astronaut: Beijing, China, 2011. (In Chinese)
15. Kim, Y.; Tanaka, K.; Lee, Y.; Matsumoto, Y. Effects of entrained air on the characteristics of a small screw-type centrifugal pump. *KSEFM J. Fluid Mach.* **2011**, *2*, 37–44.
16. Tatebayashi, Y.; Tanaka, K. Influence of meridional shape on screw-type centrifugal pump performance. In Proceedings of the ASME Fluids Engineering Division Summer Meeting, FEDSM2002-31183, Montreal, QC, Canada, 14–18 July 2002; pp. 769–776.
17. Tatebayashi, Y.; Tanaka, K.; Kobayashi, T. Thrust prediction in screw-type centrifugal pump. In Proceedings of the 4th ASME JSME Joint Fluid Engineering Conference, FEDSM2003-45105, Honolulu, HI, USA, 6–10 July 2003; pp. 621–626.
18. Cheng, X.; Lia, R. Parameter equation study for screw centrifugal pump. *Procedia Eng.* **2012**, *31*, 914–921. [[CrossRef](#)]
19. Guo, M.; Choi, Y.-D. Design and CFD analysis of a screw centrifugal pump model. *J. Korean Soc. Mar. Eng.* **2017**, *43*, 640–647. [[CrossRef](#)]
20. Franc, J.P. Partial cavity instabilities and re-entrant jet. In Proceedings of the 4th International Symposium on Cavitation, Grenoble, France; 2001.
21. Xiao, L.; Long, X. Cavitating flow in annular jet pumps. *Int. J. Multiph. Flow* **2015**, *71*, 116–132. [[CrossRef](#)]
22. Cunningham, R.G.; Hansen, A.G.; Na, T.Y. Jet Pump Cavitation. *J. Basic Eng.* **1970**, *92*, 483–492. [[CrossRef](#)]
23. Long, X.; Xu, M.; Lyu, Q.; Zou, J. Impact of the internal flow in a jet fish pump on the fish. *Ocean Eng.* **2016**, *126*, 313–320. [[CrossRef](#)]
24. Cochran, D.L.; Kline, S.J. Use of Short Flat Vanes for Producing Efficient Wide-Angle Two-dimensional Diffusers. *NASA Tech. Note* **1958**, *4309*, 1–130.
25. Kurokawa, J.; Imamura, H.; Choi, Y.-D. Effect of J-groove on the suppression of swirl flow in a conical diffuser. *J. Fluids Eng.* **2010**, *132*, 071101. [[CrossRef](#)]
26. Choi, Y.-D.; Kurokawa, J.; Imamura, H. Suppression of cavitation in inducers by J-Grooves. *J. Fluids Eng.* **2007**, *129*, 15–22. [[CrossRef](#)]
27. Choi, Y.-D.; Shrestha, U. Cavitation performance improvement of an annular jet pump by J-groove. *KSEFM J. Fluid Mach.* **2020**, *26*, 25–35. [[CrossRef](#)]
28. Shrestha, U.; Choi, Y.-D. Effect of diffuser angle and J-groove depth on improvement in suction performance of annular jet pump model. *J. Adv. Mar. Eng. Technol.* **2020**, *44*, 385–394. [[CrossRef](#)]
29. Shrestha, U.; Choi, Y.-D. Suction performance improvement of an annular jet pump by J-Groove passage shape optimization. *J. Mech. Sci. Technol.* **2021**, *35*, 5517–5527. [[CrossRef](#)]
30. Hoang, T.H.M.; Truong, V.A.; Shrestha, U.; Choi, Y. Optimization of the Meridional Plane Shape Design Parameters in a Screw Centrifugal Pump Impeller. *KSEFM J. Fluid Mach.* **2021**, *24*, 15–25. [[CrossRef](#)]
31. ANSYS. *ANSYS CFX Documentation*; ANSYS Inc.: Canonsburg, PA, USA, 2017.
32. Celik, I.B.; Ghia, U.; Roache, P.J.; Freitas, C.J. Procedure for estimation and reporting of uncertainty due to discretization in CFD applications. *J. Fluids Eng.-Trans. ASME* **2008**, *130*, 078001.

-
33. Franc, J. The Rayleigh-Plesset equation: A simple and powerful tool to understand various aspects of cavitation. In *Fluid Dynamics of Cavitation and Cavitating Turbopumps*; Springer: Berlin/Heidelberg, Germany, 2007; pp. 1–41.
 34. Xu, K.; Wang, G.; Wang, L.; Yun, F.; Sun, W.; Wang, X.; Chen, X. CFD-Based Study of Nozzle Section Geometry Effects on the Performance of an Annular Multi-Nozzle Jet Pump. *Processes* **2020**, *8*, 133. [[CrossRef](#)]